The Astrophysical Journal, 804:149 (10pp), 2015 May 10 doi:10.1088/0004-637X/804/2/149

INVESTIGATING Hα, UV, AND IR STAR-FORMATION RATE DIAGNOSTICS FOR A LARGE SAMPLE OF $z \sim 2$ GALAXIES

Irene Shivaei[1,4], Naveen A. Reddy[1,5], Charles C. Steidel[2], and Alice E. Shapley[3]

[1] Department of Physics and Astronomy, University of California, Riverside, 900 University Avenue, Riverside, CA 92521, USA

[2] Cahill Center for Astronomy and Astrophysics, California Institute of Technology, 1216 E. California Blvd., MS 249-17, Pasadena, CA 91125, USA

[3] Department of Physics & Astronomy, University of California, Los Angeles, 430 Portola Plaza, Los Angeles, CA 90095, USA

Received 2014 August 26; accepted 2015 March 12; published 2015 May 12

ABSTRACT

We use a sample of 262 spectroscopically confirmed star-forming galaxies at redshifts $2.08 \leqslant z \leqslant 2.51$ to compare Hα, ultraviolet (UV), and IR star formation rate (SFR) diagnostics and to investigate the dust properties of the galaxies. At these redshifts, the Hα line shifts to the K_s band. By comparing K_s-band photometry to underlying stellar population model fits to other UV, optical, and near-infrared data, we infer the Hα flux for each galaxy. We obtain the best agreement between Hα- and UV-based SFRs if we assume that the ionized gas and stellar continuum are reddened by the same value and that the Calzetti attenuation curve is applied to both. Aided with MIPS 24 μm data, we find that an attenuation curve steeper than the Calzetti curve is needed to reproduce the observed IR/UV ratios of galaxies younger than 100 Myr. Furthermore, using the bolometric SFR inferred from the UV and mid-IR data ($\mathrm{SFR_{IR}+SFR_{UV}}$), we calculated the conversion between the Hα luminosity and SFR to be $(7.5 \pm 1.3) \times 10^{-42}$ for a Salpeter initial mass function, which is consistent with the Kennicutt conversion. The derived conversion factor is independent of any assumption of the dust correction and is robust to stellar population model uncertainties.

Key words: galaxies: evolution – galaxies: high-redshift – galaxies: star formation

1. INTRODUCTION

One of the most important diagnostics in understanding the evolution of galaxies is the star formation rate (SFR). The evolution of the SFR of galaxies can give clues as to how galaxies were enriched with heavy elements and how they build up their stellar mass through cosmic time, and it helps us to understand the bolometric output of galaxies. At redshift $z \sim 2$, when the universe was just ∼3 Gyr old, star formation activity in the universe was at its peak and galaxies were in the process of assembling most of their stellar mass (see Reddy & Steidel 2009; Bouwens et al. 2010; Shapley 2011; Madau & Dickinson 2014). Studying this critical epoch is essential to gaining a better understanding of the evolution of the progenitors of the local galaxy population.

The ultraviolet (UV) continuum (1500–2800 Å) intensity of a galaxy is one of the most commonly used diagnostics for the SFR as it is observable over a wide range of redshifts and intrinsic luminosities. It is sensitive to massive stars ($M_* \gtrsim 5\ M_\odot$), making it a direct tracer of current SFR. By extrapolating the formation rate of massive stars to lower masses, for an assumed form of the initial mass function (IMF), one can estimate the total SFR (Madau et al. 1998). Another widely used diagnostic for measuring the SFR is nebular emission, with Hα being the most common because of its higher intensity compared to the other hydrogen recombination lines such as Hβ, Paα, Paβ, etc., and it is easier to interpret than the Lyα line. Hα is an "instantaneous" tracer of SFR because it is sensitive only to the most massive stars ($M_* \gtrsim 10\ M_\odot$). However, it becomes more challenging to observe Hα from the ground at $z \gtrsim 1$ because the line is redshifted to the near-IR, where the terrestrial background is much higher than at optical wavelengths.

The main disadvantage of using UV/optical luminosities as tracers of the SFR is their sensitivity to dust attenuation. The dust absorption cross section is larger for shorter wavelengths, and choosing the appropriate attenuation curve to correct the observed luminosities plays an important role in determining intrinsic physical quantities. Aside from the assumed attenuation curve, the geometry of dust with respect to the stars can lead to different color excesses, $E(B-V)$, between the ionized gas and the stellar continuum. $E(B-V)$ is the color excess measured between the B and V bands, $E(B-V) \equiv A_B - A_V$, where A_λ is the total extinction at wavelength λ in magnitudes. In particular, the nebular recombination lines arise from the H II regions around the most massive O and early-type B stars (with masses of $M_* \gtrsim 10\ M_\odot$ and main-sequence lifetimes of $\lesssim$10 Myr). On the other hand, for a Salpeter IMF, solar metallicity, and a constant or rising star formation history, the UV continuum in starburst galaxies originates from stars over a broader range of mass that includes later-type B stars with lifetimes $\lesssim$100 Myr (Kennicutt 1998; Madau & Dickinson 2014). These older non-ionizing stars have more time to migrate to regions of lower dust density in the galaxy, while H-ionizing stars with shorter lifetimes do not have enough time to escape from their dusty birthplace or let the parent molecular clouds dissipate. As a result, the nebular lines can be subject to a higher degree of reddening than the UV continuum.

Calzetti et al. (1994) found that the nebular emission is more attenuated than the stellar continuum at the same wavelengths for a sample of local UV-bright galaxies. Subsequently, Calzetti et al. (2000) studied a similar sample of local galaxies and argued that the *color excess* is 2.27 times larger for the nebular emission lines than for the stellar continuum. This relationship was derived under the assumption that the Calzetti curve is applied to the stellar continuum and a Galactic extinction curve is applied to the nebular emission lines. In a

[4] NSF Graduate Research Fellow.

[5] Alfred P. Sloan Research Fellow.

separate study, Cid Fernandes et al. (2005) found that for an SDSS sample of ~50,000 galaxies, $A_{V,\mathrm{nebular}} \sim 1.8\,A_{V,\mathrm{stellar}}$, both assuming a Cardelli et al. (1989) extinction curve.

There have been several studies of relative attenuation of the stellar continuum and nebular regions in high-redshift galaxies. In most of the high-redshift studies, the Calzetti curve is assumed for both the nebular and stellar regions. Frequently, the Calzetti et al. (2000) relation between the stellar and nebular $E(B-V)$ is used to correct the nebular lines, while this relation was originally derived based on using a Galactic extinction curve for the nebular lines. At present it is unclear what type of attenuation curve should be applied to the nebular regions. These issues are discussed in detail in Steidel et al. (2014).

At $z \sim 2$, Förster Schreiber et al. (2009) selected a sample from various imaging surveys in the optical, near-IR, mid-IR, and sub-millimeter regime, with SED-derived SFRs of ~10–1000 $M_\odot$ yr^{-1} and stellar masses $\gtrsim 10^{10}\,M_\odot$, assuming a Chabrier IMF. In their study, the predicted Hα luminosities from the best-fit SED models for 62 galaxies were compared with the observed line luminosities measured from integral field spectroscopy. The latter were then corrected for reddening assuming the A_V returned from stellar population modeling of their galaxies. Förster Schreiber et al. (2009) found that assuming a factor of two redder color excess toward the H II regions relative to the stellar continuum yielded the best agreement between the predicted and observed Hα luminosities. Similarly, Wuyts et al. (2011) investigated 25 star-forming galaxies at $z \sim 2$ and compared the Hα SFRs, dust-corrected by the Calzetti attenuation curve, with the SED-modeled SFRs. They showed that Hα SFRs are consistent with the SED SFRs, provided that $E(B-V)_{\mathrm{neb}} = 2.27E(B-V)_{\mathrm{stellar}}$ when assuming the Calzetti curve for both.

Muzzin et al. (2010) presented two galaxies at redshifts $z = 2.122$ and 2.024 and added 10 other galaxies at similar redshifts from van Dokkum et al. (2005), Kriek et al. (2007), and Kriek et al. (2009) to compare $A_{V,\mathrm{nebular}}$ derived from the Balmer decrement ($F(\mathrm{H}\alpha)/F(\mathrm{H}\beta)$) with $A_{V,\mathrm{stellar}}$ derived from the SED models, both assuming the Calzetti curve. The only two galaxies with detected Hβ line measurements showed evidence for higher nebular attenuation, but about half of the non-detections were consistent with equal attenuation for the nebular and stellar regions. In Yoshikawa et al. (2010), Hα attenuation was investigated through several comparisons for a sample of optically selected star-forming galaxies at $z \sim 2$. Aided with near-infrared spectroscopic observations, Yoshikawa et al. (2010) used the Balmer decrement along with the Calzetti curve to correct the Hα SFR. The dust-corrected SFR was then compared with the Hα SFR corrected by the SED color excess and also with the SFRs inferred from UV, IR, radio, and X-ray. The comparisons yield contradictory results. Their analysis favored a higher nebular color excess for galaxies with larger intrinsic SFRs.

In separate studies, Erb et al. (2006b) and Reddy et al. (2010) used a large sample of UV-selected galaxies at $z \sim 2$ and corrected both the Hα and UV SFRs with the color excess derived from the best-fit SED models and applied the Calzetti attenuation curve. They showed that using different color excesses for the continuum and lines generally resulted in Hα-inferred SFRs that overpredicted those calculated from the dust-corrected UV emission and direct IR measurements.

The apparently conflicting results mentioned above may be reconciled if the relation between the nebular and stellar color excesses depends on the physical properties of galaxies, such as their SFRs (Yoshikawa et al. 2010), specific SFRs (Wild et al. 2011), or metallicity (Zeimann et al. 2014). For example, Wild et al. (2011) showed that the ratio of the line optical depth to the continuum optical depth decreases with increasing sSFR and at sSFR $\sim 10^{-9}$ yr^{-1} the line-to-continuum optical depth ratio reaches the Calzetti et al. (2000) ratio assuming the Wild et al. (2011) attenuation curve. Price et al. (2014) investigated the attenuation of the nebular regions at $z \sim 1.5$ using the Balmer decrement from stacked *Hubble Space Telescope* (*HST*) grism spectra assuming the Calzetti curve and found no strong trend of $A_{v,\mathrm{neb}}/A_{v,\mathrm{stellar}}$ with SFR or sSFR. In the Price et al. (2014) study, at sSFR $\sim 10^{-8.5}$ yr^{-1} the ratio is consistent with 1.

The primary goal of this paper is to understand the relationship between the UV and Hα emission in high-redshift star-forming galaxies, with a large sample that is immune to uncertainties in slit-loss corrections that affect the Hα flux estimation (see Erb et al. 2006b; Yoshikawa et al. 2010), the small sample sizes inherent in previous spectroscopic studies of Hα (Kriek et al. 2007; Muzzin et al. 2010), and not subject to the bias of selecting high equivalent width objects from narrowband selected samples (Garn et al. 2010). We consider in our analysis only spectroscopically confirmed galaxies, enabling us to estimate the Hα flux from broadband photometric excess techniques without the additional uncertainties that plague photometric redshifts (Wuyts et al. 2011).

The impact of nebular lines on the broadband photometry was known and studied for many years (e.g., Guiderdoni & Rocca-Volmerange 1987; Fioc & Rocca-Volmerange 1997; Zackrisson et al. 2008; de Barros et al. 2014). Using the photometric excesses to determine the line strengths was pioneered by Shim et al. (2011), where they showed that the excess in *Spitzer*/IRAC 3.6 μm relative to the SED model continuum is due to the redshifted Hα emission line for their sample of galaxies at $3.8 < z < 5.0$. Stark et al. (2013) also investigated a sample of galaxies at the same redshift range of Shim et al. (2011) and inferred the Hα emission line strengths by comparing the observed flux in *Spitzer*/IRAC 3.6 μm band and the continuum flux as expected from the SED model. Following that, Schenker et al. (2013) verified the photometric excess technique by applying it to a small sample of nine galaxies at $3.0 < z < 3.8$; for eight galaxies the [O III] line fluxes inferred by the same technique as Stark et al. (2013) were within a factor of 2.5 of the spectroscopically measured [O III] fluxes.

An additional advantage of our study is that we include IR data to independently assess the dust-obscured SFR. Comparing Hα, UV, and IR-inferred SFRs in a statistical sense allows us to understand how to correct extinction-sensitive measures of SFR for the effects of dust.

The outline of this paper is as follows. In Section 2 we discuss the properties of our sample, the assumptions that have been made to model the stellar populations using the rest-frame UV to near-IR photometry, the *Spitzer*/MIPS photometry, and the stacking method. A detailed description of how we estimated the Hα line flux is provided in Section 3. The analysis of the MIPS 24 μm data and IR luminosities is described in Section 4. In Section 5 we compare the two different tracers of SFR—Hα and UV—and discuss the dust

correction recipe most consistent with our measured values. Section 6 focuses on combining SFR diagnostics (e.g., Hα and UV with IR) to deduce bolometric SFRs. The results are summarized in Section 7. Throughout this paper, a Salpeter (1955) IMF is assumed and a cosmology with $H_0 = 70$ km s^{-1} Mpc^{-1}, $\Omega_\Lambda = 0.7$, and $\Omega_m = 0.3$ is adopted. All magnitudes are given in the AB system (Oke & Gunn 1983).

2. SAMPLE

2.1. Sample Selection and Optical Photometry

The galaxies used in this study are drawn from a parent sample that is part of an imaging and spectroscopic survey of UV-selected galaxies at $z \sim 2$–3 (Steidel et al. 2004; Reddy et al. 2012b). The galaxies were selected based on the BX, BM, and Lyman break galaxy rest-UV color criteria (Steidel et al. 2003, 2004; Adelberger et al. 2004), where U_{nGR} optical data were obtained with the Palomar Large Format Camera or Keck Low Resolution Imaging Spectrograph (LRIS; Steidel et al. 2003, 2004). Rest-UV spectroscopic follow-up with Keck/LRIS was conducted for galaxies brighter than $R = 25.5$ (Steidel et al. 2003, 2004). Near-IR J and K_s imaging was obtained using the Palomar/WIRC and *Magellan*/PANIC instruments (Shapley et al. 2005; Reddy et al. 2012b). H-band (F160w) data were obtained with the *HST* WFC3 camera (Law et al. 2012; Reddy et al. 2012b). All galaxies in the sample have coverage in at least one of the four *Spitzer*/IRAC channels (3.6, 4.5, 5.8, and 8.0 μm; Reddy et al. 2006a, 2012b). The objects are located in the GOODS-North field and 11 additional fields that were primarily selected to have one or more relatively bright background QSOs for studying the interface between the intergalactic medium and galaxies at $z \sim 2$–3 (Steidel et al. 2004, 2010).

Out of the final sample of 2283 objects with spectroscopically confirmed redshifts, a subset of galaxies is selected based on the following criteria: (1) the galaxy must be covered by the K-band imaging, (2) it must have a redshift in the range $2.08 \leqslant z \leqslant 2.51$ so that the Hα line falls into the K_s band, and (3) it must be detected in at least two of the IRAC channels or one of the IRAC channels and either J or F160W bands. The third condition ensures a more robust estimate of the stellar mass and the continuum level at 6564 Å. Furthermore, AGNs (making up ≈9% of the parent sample) were identified by either strong UV emission lines (e.g., Lyα, C IV) or a power-law SED through the IRAC bands. These AGNs are removed from our sample. Eventually, 262 galaxies remain that satisfy the aforementioned criteria.

2.2. Stellar Population Modeling

For each galaxy in our sample, the best-fit stellar population model is found by using the rest-frame UV through near-IR broadband photometry. As mentioned above, all the galaxies in our sample have spectroscopically confirmed redshifts, thus removing a key degeneracy in the modeling of the stellar populations. In addition, for a better estimation of stellar mass and age, all galaxies in our sample have at least two detections longward of the 4000 Å break—excluding K_s band.

S. Charlot & G. Bruzual (2007, in preparation) models with a Salpeter (1955) IMF and solar metallicities are used for the fitting. For each individual galaxy, different star formation histories are assumed, including constant, exponentially declining, and exponentially rising with characteristic timescales of $\tau = 10$, 20, 50, 100, 200, 500, 1000, 2000, and 5000 Myr for exponentially declining and $\tau = 100$, 200, 500, 1000, 2000, and 5000 Myr for exponentially rising histories. Ages are allowed to vary between 50 Myr and the age of the universe at the redshift of each galaxy. The >50 Myr limit corresponds to the typical dynamical timescale of star-forming galaxies at $z \sim 2$ as inferred from velocity dispersion and size measurements of these galaxies (Reddy et al. 2012b). For interstellar dust obscuration, the Calzetti et al. (2000) attenuation curve is used, allowing $E(B-V)$ to vary between 0.0 and 0.6. The χ^2 values have been determined for each set of observed broadband and model magnitudes. The best-fit model is determined through χ^2 minimization. There is generally no significant difference between the best-fit χ^2 values of the six different population models (constant, exponentially rising, and exponentially declining star formation histories, for each considering all ages and ages greater than 50 Myr). As previous studies have shown, the assumption of declining star formation histories at these redshifts results in systematically lower SED-inferred SFRs compared to the observed IR+UV SFRs (Wuyts et al. 2011; Reddy et al. 2012b). Furthermore, Reddy et al. (2012b) showed that assuming a constant star formation history for $z \sim 2$ galaxies predicts specific SFRs (SFR/M_*) at higher redshifts ($z \sim 2.6$) that are substantially larger than the observed values. Given these, we adopt the models that assume exponentially rising star formation histories with ages greater than 50 Myr.

The SED models used to fit the observed magnitudes do not include nebular emission lines. For example, the Hα line can significantly affect the photometry, and we use its contribution to the K band to estimate the Hα line flux. The [O III] emission line is the other strong line that falls into the F160W filter given the redshift range of our galaxies. Only 20% of the galaxies have F160W observations, for which we did not correct the broadband photometry for the contamination. The SED-inferred SFR of these galaxies is consistent with the SFR (UV) estimates within the uncertainties. At this redshift, J band is contaminated by the [O II] emission line, but this line is generally weaker than the Hα line, and its effect on the SED-inferred SFRs is negligible compared to the uncertainties.[6]

2.3. MIPS Data

To further investigate the bolometric properties of our sample, we use *Spitzer*/MIPS 24 μm wherever available. Out of 12 fields, GOODS-North (Dickinson et al. 2003) and four other fields (Q1549, Q1623, Q1700, and Q2343; Reddy & Steidel 2009) have MIPS 24 μm coverage to a typical 3σ depth of 10–15 μJy.

Photometry on 24 μm images is performed by using point-spread function (PSF) fitting with priors determined by the locations of the objects in the higher-resolution IRAC images (IRAC data exist in all fields). A 40 × 40 pixel region centered on each target is extracted with pixel size of 1.″2. PSFs are then fitted simultaneously to all known sources in the sub-image and one random background position. This procedure is repeated many times to obtain sufficient statistics for proper background estimation based on the random background flux measurements. The other source of uncertainty is Poisson noise, which

[6] For galaxies with similar SFRs at $z \sim 2$, the typical [O II] line flux is $\sim 6 \times 10^{-17}$ erg s^{-1} cm^{-2} (Kriek et al. 2014). The ratio of the [O II] flux to the typical J-band flux errors in our observations is only ∼0.07.

for objects in our sample is negligible compared to the background dispersion. We remove objects whose photometry may be compromised due to blending with nearby sources, using the criteria specified in Reddy et al. (2010). This results in 115 galaxies with secure PSF fits.

Out of 115 objects with MIPS data, 47 are detected with signal-to-noise ratio (S/N) $\geqslant 3$. Undetected objects, those with S/N < 3, are considered either using survival analyses or through stacking of the 24 μm data.

2.3.1. Stacking Method

Throughout the paper, we employ a stacking method to determine the median 24 μm fluxes of objects that are individually detected and undetected, following the procedures described in Reddy et al. (2010, 2012a). We performed aperture photometry on the stacked images and applied an aperture correction based on the 24 μm PSF. The average background level and noise were determined by placing many apertures of the same size used for the stacked signal at random positions in the stacked image and measuring the average flux level and dispersion in flux of these "background" apertures. Furthermore, we used bootstrap resampling simulations to estimate the dispersion in the fluxes of objects contributing to each stack. This was accomplished by creating 100 samples of random images in each bin and measuring the standard deviation of the median stacked fluxes. The intrinsic dispersion in the stacked flux is larger than the background error by a factor of $\sim$2.

3. Hα AND UV LUMINOSITY

3.1. Hα Fluxes and Equivalent Widths

Using the procedure discussed in Section 2.2, we fit all the photometry, excluding K_s band, in order to determine the continuum level at 6564 Å. The continuum magnitude is calculated by multiplying the best-fit SED model by the K_s filter transmission curve. The difference between the observed K_s-band magnitude and the continuum magnitude is used to extract the Hα line flux as follows. The observed K_s magnitude is considered as the sum of the continuum and the Hα fluxes, while the SED-inferred K_s magnitude represents only the continuum flux. Assuming a Gaussian form for the redshifted Hα line, the change between these fluxes will yield the Hα flux (Figure 1):

$$\frac{\int \frac{d\nu}{\nu} f_{\mathrm{H}\alpha}(\nu) T_K(\nu)}{\int \frac{d\nu}{\nu} T_K(\nu)} = 10^{\frac{(m_{\mathrm{obs}}+48.6)}{-2.5}} - 10^{\frac{(m_{\mathrm{SED}}+48.6)}{-2.5}}. \quad (1)$$

Here, $f_{\mathrm{H}\alpha}(\nu)$ is the flux density of the Hα line in units of erg s^{-1} cm^{-2} Hz^{-1}, $T_K(\nu)$ is the K_s filter transmission curve, and m_{obs} and m_{SED} are the observed and the continuum magnitudes, respectively. The Hα flux is corrected for contamination from the [N II] line based on the mass-dependent [N II]-to-Hα flux ratios of Erb et al. (2006a). The stellar masses are determined from the SED models, and the corresponding [N II] line contamination, as listed in Table 1, is used to correct the Hα flux. The SFRs are then calculated using the Kennicutt (1998) relation to convert the Hα line luminosity to an SFR.

There are three main sources of uncertainty in the derived Hα fluxes. The largest uncertainty is the photometric error. The typical error in the observed K_s-band magnitude is $\simeq$0.27. The second source of uncertainty is the [N II] correction. The uncertainty on the Erb et al. (2006a) [N II]-to-Hα line ratios (see Table 1) is added in quadrature to the photometric error. The third source of uncertainty is the error associated with the continuum flux. In order to account for this uncertainty, we estimated the continuum flux at 6564 Å from the best-fit model assuming six different star-formation histories: exponentially rising, exponentially declining, and constant, for each considering all ages and ages greater than 50 Myr. For 94% of the galaxies the difference in the mean of the continuum fluxes assuming different star-formation histories to those assuming a rising star-formation history with ages $\geqslant$50 Myr is less than 0.1 mag. The average error in the estimated continuum magnitude is $\sim$0.05 mag, which is negligible compared to the observed K_s -band magnitude errors. Combining the three sources of uncertainty discussed above yields a typical relative error in Hα flux of $\sim$0.29.

The equivalent width of the Hα line is estimated by dividing the Hα flux derived from Equation (1) by the continuum flux density at the wavelength of the Hα line:

$$(1+z)\mathrm{EW}_0 = \frac{F_{\mathrm{H}\alpha}}{f_\lambda^{\mathrm{cont}}}. \quad (2)$$

The $f_\lambda^{\mathrm{cont}}$ is the continuum flux density in units of erg s^{-1} cm^{-2} Å^{-1} that is estimated through the best-fit SED model, $F_{\mathrm{H}\alpha}$ is the Hα line flux in erg s^{-1} cm^{-2}, z is the redshift of the galaxy, and EW_0 is the rest-frame equivalent width in Å.

We define whether a galaxy has a "detected" Hα line according to the following. Galaxies whose K_s-band photometry exceeds the continuum level by more than the K_s-band magnitude error are referred to as "Hα detections." Galaxies where the K_s-band photometry is consistent with the continuum level to within 1σ are referred to as "Hα non-detections," and an upper limit of 1σ above the measured K photometry is used for these objects. Out of 262 galaxies in our sample, 149 are detections and 94 are non-detections. There are 19 objects with K_s magnitudes fainter than the continuum by more than 1σ. We removed these galaxies from our discussion due to their K_s photometry being inconsistent with the photometry from adjacent bands.

As discussed in Section 1, our method of computing Hα fluxes and EWs has the advantage of being immune to slit-loss corrections. Our sample covers a wide range of Hα fluxes and EWs. Figure 2 shows the distribution of Hα EWs and fluxes as a function of the K_s magnitude 1σ uncertainty. The detection of Hα with the method adopted here depends on both the Hα line flux and the brightness of the continuum at 6564 Å. As we have defined detections to be those objects where the K_s magnitude exceeds the continuum level by more than 1σ, the number of undetected objects increases for objects that are fainter in the continuum (Figure 2).

The Hα observed fluxes of 44 objects in common with the Erb et al. (2006b) spectroscopic sample are compared in Figure 3. The Erb et al. (2006b) spectroscopic fluxes are multiplied by a factor of two to account for slit losses and the aperture used to extract the spectra (Erb et al. 2006b; Reddy et al. 2010). The slit-loss correction factor applied to the spectroscopic fluxes depends on various factors such as the accuracy of the astrometry, the size of the object convolved with the seeing at the time of observation in comparison with the size of the slit, and the accuracy of the mask alignment

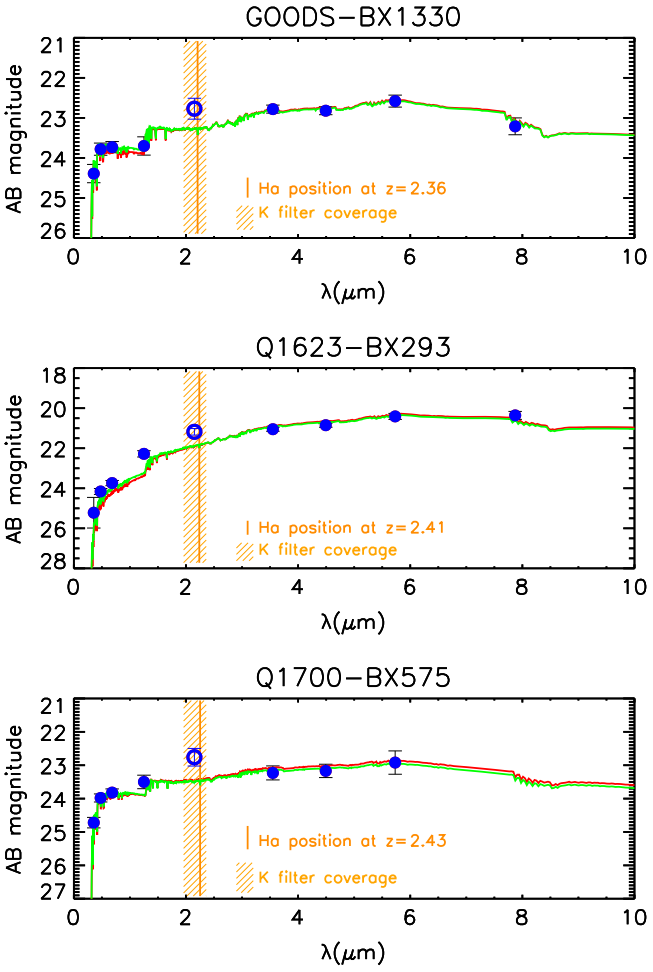

Figure 1. Best-fit SED models for three objects in our sample: BX1330 in GOODS-North (top), BX293 in Q1623 (middle), and BX575 in Q1700 (bottom). All the models assume an exponentially rising star-formation history, with a lower limit in age of 50 Myr. The K_s-band data are shown with an open circle in each plot. The green and red lines show the best-fit models when we exclude and include, respectively, the K-band photometry in the fitting. The two fits are similar because the K_s photometry is down-weighted in the fitting due to larger measurement errors. The vertical orange line shows the position of the redshifted Hα line. The dashed area represents the K_s filter coverage. At redshifts of $z \sim 2.08-2.50$, the K_s filter is affected by the Hα emission line, and the difference between the K_s-band flux and the underlying stellar population model can be used to estimate the line flux.

Table 1
Hα Flux Corrections for [N II] Contamination[a]

Mass Range ($10^{10}\,M_\odot$)[b]	$N2$[c]
<0.88	<-1.22
0.88–2.00	$-1.00^{+0.07}_{-0.09}$
2.00–3.69	$-0.85^{+0.05}_{-0.06}$
3.69–6.03	$-0.78^{+0.05}_{-0.05}$
6.03–8.82	$-0.66^{+0.03}_{-0.04}$
>8.82	$-0.56^{+0.02}_{-0.02}$

[a] Based on Erb et al. (2006a).
[b] Assuming a Salpeter (1955) IMF.
[c] $N2 \equiv \log\left(F([\mathrm{NII}])/F(\mathrm{H}\alpha)\right)$.

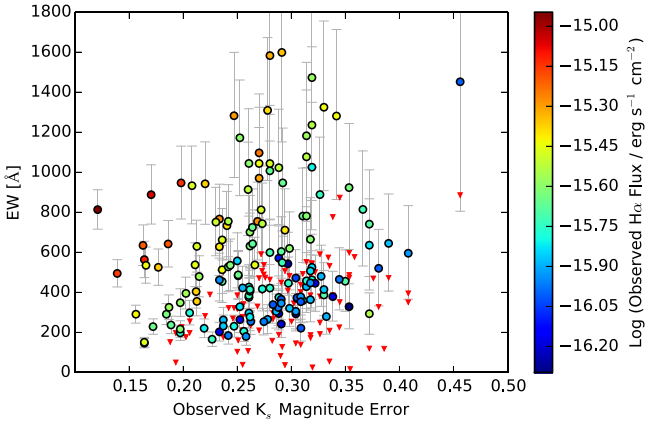

Figure 2. Estimated Hα rest-frame equivalent widths as a function of the error of the observed K_s-band magnitude. The circles are detected galaxies and are color coded based on their observed Hα fluxes (uncorrected for extinction). The red triangles show 1σ upper limits. Detecting the Hα emission requires that the observed K_s magnitude lies more than 1σ above the underlying continuum, where 1σ is defined by the K_s magnitude error. The K_s magnitude includes both the light from the Hα emission line and the brightness of the continuum at 6564 Å. There is a tight correlation between the continuum brightness and the K_s magnitude error; the fainter continuum results in larger uncertainty in the observed magnitude. As a result, there are more undetected objects with large K_s-band errors. On the other hand, the brightest Hα objects have bright continuum and small K_s-band uncertainties. The deficiency of objects in the upper-left corner is mainly because very bright Hα objects that also have bright continuum are rare.

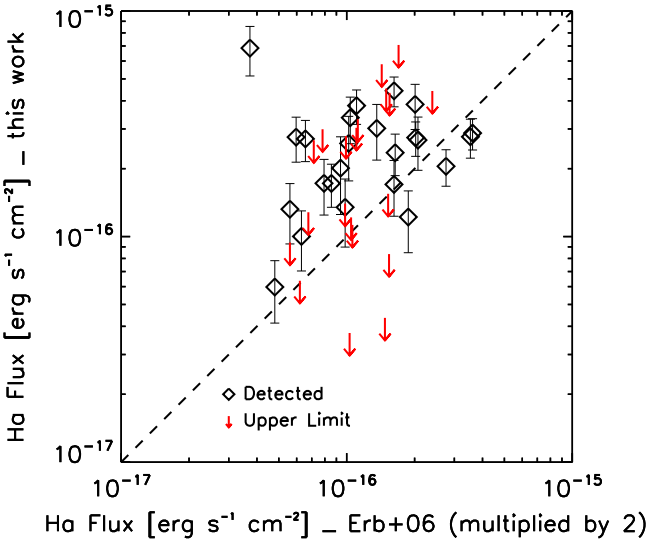

Figure 3. Comparison of observed Hα fluxes of the objects in common between our sample and that of Erb et al. (2006b). The diamonds are the detected objects, and downward arrows show 1σ upper limits, as discussed in the text. The fluxes are measured based on the difference between the observed and the continuum K_s magnitudes predicted from the best-fit model. The error bars are dominated by the uncertainty in the observed K_s photometry. The Erb et al. (2006b) spectroscopic fluxes are multiplied by a factor of 2 to account for slit losses. The dashed line denotes the one-to-one relationship.

during the observation. As noted in Erb et al. (2006b), the factor of two slit-loss correction is an average estimate, and the slit losses will of course vary from object to object, likely accounting for some of the scatter in Figure 3. On the other hand, while broadband photometry has its advantages, our K_s -band measurements suffer from a larger measurement (random) uncertainty relative to the other methods given the depth of our ground-based images. Although most of the

detected Hα fluxes in this study (the black symbols in Figure 3) are higher than the spectroscopic fluxes, about half of the sample is estimated as upper limits (the red arrows). Considering both the detections and non-detections, the broadband estimated fluxes are generally consistent with the spectroscopic fluxes. To quantify the degree of the correlation, we conduct a generalized Kendall's tau (τ) statistic. The generalized Kendall's τ rank correlation coefficient is a non-parametric test that permits non-detections in both variables (here, our estimated Hα fluxes). Kendall's τ correlation coefficient for our flux estimation with the Erb et al. (2006b) measurements, excluding the one outlier object, is $\tau = 0.17$, with significance of p-value $= 0.11$.

3.2. UV Luminosities and SFRs

UV luminosities are calculated using the fluxes of the best-fit SED models at 1700 Å. The Kennicutt (1998) relation to convert the UV luminosity (over the wavelength range 1500–2800 Å) to SFR applies only to galaxies where star formation proceeds for $\gtrsim$100 Myr. However, there are galaxies in our sample with inferred ages between 50 and 100 Myr. For these younger galaxies, we used an age- and star-formation-history-dependent relation in the conversion of the UV luminosity to SFR, as discussed in Reddy et al. (2012b). The age-dependent conversion resulted in UV SFRs that are at most 14% larger than the Kennicutt (1998) SFRs for young galaxies. Throughout this analysis, we also use SFRs inferred from the best-fit SED models. As expected, within the uncertainties, the SED SFRs are highly correlated with dust-corrected UV SFRs.

4. THE IR LUMINOSITY AND BOLOMETRIC PROPERTIES

To estimate the bolometric luminosities of galaxies in our sample, we infer the infrared luminosity (integrated between 8 and 1000 μm) as discussed below, and we add this to the unobscured UV luminosity (i.e., observed UV luminosity; Section 3.2), as in Reddy et al. (2010).

Infrared luminosities, $L_{\rm IR}$, are estimated by using the *Spitzer*/MIPS 24 μm observations. The 24 μm band is sensitive to the rest-frame 7.7 μm PAH emission, which correlates with $L_{\rm IR}$ (e.g., Chary & Elbaz 2001; Dale & Helou 2002; Elbaz et al. 2011). To convert observed 24 μm magnitudes to total IR luminosity ($L_{\rm IR}$), we used several dust SED templates, including those of Chary & Elbaz (2001), Dale & Helou (2002), and Rieke et al. (2009). Luminosities determined from the rest-frame 8 μm flux density alone, regardless of the dust template used, tend to overpredict L(IR), particularly for LIRGs (e.g., Reddy et al. 2012a) and ULIRGs (e.g., Nordon et al. 2010; Magnelli et al. 2011). In order to account for the luminosity-dependent overestimation of the derived L(IR), we use a correction equation described in Reddy et al. (2012a). The correction is calculated by comparing the L(IR) computed from 24, 100, 160 μm, and 1.4 GHz fluxes, and the L(IR) determined solely from 24 μm data for a similarly selected sample of galaxies:

$$\log L_{\rm IR}(\text{all data}) = 0.537 \times \log L_{\rm IR}(24\ \mu\text{m}) + 5.136. \quad (3)$$

All luminosities are in $L_\odot$.

Equation (3) is based on the Chary & Elbaz (2001) models. There is a factor of ~2 variation in L(IR) derived from 24 μm data using Dale & Helou (2002) and Rieke et al. (2009) dust templates (e.g., see Reddy et al. 2012a). However, once corrected using the appropriate equations similar to Equation (3), all the templates result in L(IR) estimates that are consistent with each other and with the L(IR) computed from 24, 100, 160 μm, and 1.4 GHz fluxes, within the uncertainties of the measured IR luminosity as explained in Section 2.3 (see also Reddy et al. 2012a). In the subsequent analysis, we use infrared luminosities inferred from the Chary & Elbaz (2001) templates.

The IR luminosity is converted to IR (dust-obscured) SFRs using the Kennicutt (1998) relation. The sum of IR- and UV-inferred SFRs is then used to estimate the bolometric SFRs.

5. DUST ATTENUATION OF THE NEBULAR REGIONS AND STELLAR CONTINUUM

SFRs inferred from the UV luminosity and the Hα fluxes are shown in the left panel of Figure 4. Without dust corrections, the UV and Hα SFRs have a large discrepancy due to the smaller dust absorption cross section at 6564 Å relative to that at 1700 Å (see the inset panel in Figure 4). The main left panel of Figure 4 shows Hα and UV SFRs, both corrected for dust attenuation based on the Calzetti attenuation curve and assuming that the same color excess, $E(B-V)$, as derived from the best-fit SED model, applies to the stellar continuum and the nebular regions. To better quantify the mean trend, measurements have also been performed in bins of UV dust-corrected SFR (filled circles in Figure 4). The bins are $\Delta\log(\mathrm{SFR_{UV,corrected}}) = 0.3$ dex wide. For all the galaxies in each bin, regardless of their redshift, we calculate the median flux densities in the observed filters. With the new set of median fluxes, the best-fit stellar population model is determined through χ^2 minimization for the mean redshift of the galaxies in each bin. The Hα and UV luminosities are then derived from the stacked SED in the same way as for individual galaxies (see Section 3). Reported errors are calculated based on the 1σ standard error of the mean of the K_s magnitudes contributing to each bin.

The appropriate dust corrections to apply to the nebular emission lines is still a subject of debate, as discussed in Section 1. The attenuation of the nebular lines and the UV stellar continuum are not completely decoupled as both arise from dust around massive stars. On the other hand, whether the color excess is the same for the nebular and stellar regions (e.g., Erb et al. 2006b; Reddy et al. 2010) or not (e.g., Calzetti et al. 2000; Förster Schreiber et al. 2009; Garn et al. 2010) in high-redshift galaxies has yet to be fully investigated.

Calzetti et al. (2000) found that $E(B-V)_{\rm stel} = 0.44 \times E(B-V)_{\rm neb}$ for a sample of local star-forming galaxies. In the absence of direct measurements of the nebular color excess (e.g., via the Balmer decrement), this relationship can in principle be used to estimate the nebular color excess and apply a dust correction to the Hα line; e.g.,

$$\begin{aligned} A_{\rm H\alpha} &= \kappa_{\rm Gal}(\rm H\alpha) E(B-V)_{\rm nebular} \\ &= 2.27\ \kappa_{\rm Gal}(\rm H\alpha) E(B-V)_{\rm stellar} \\ &= 2.27 \times 2.52\, E(B-V)_{\rm stellar} \\ &= 5.72\, E(B-V)_{\rm stellar}, \end{aligned} \quad (4)$$

where $\kappa_{\rm Gal}$ is the Cardelli et al. (1989) Galactic extinction curve, assuming that the nebular regions in the high-redshift galaxies abide by such a dust curve. $A_{\rm H\alpha}$ is the absolute

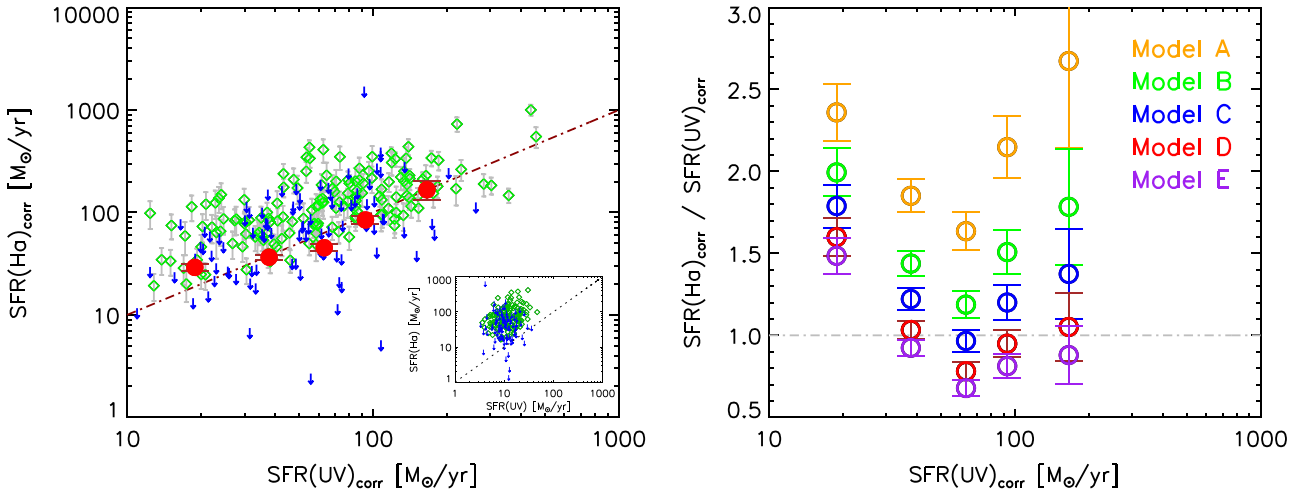

Figure 4. *Left:* comparison of SFR(Hα) and SFR(UV), both corrected for dust assuming the Calzetti attenuation curve and assuming that the same color excess applies for the stellar and nebular regions. The uncorrected values are shown in the inset panel. Green diamonds denote "detected" objects, those whose K_s-band magnitudes are more than 1σ brighter than the continuum. Blue arrows show the remaining "undetected" objects. Red filled circles are the results of stacked SEDs in bins of dust-corrected SFR(UV), including both the detected and undetected objects. Undetected objects bring the stacks lower than the average of the individually detected green diamonds. The dashed lines indicate the one-to-one relationships. *Right:* ratio of $\mathrm{SFR(H}\alpha)_{\mathrm{corrected}}$ to $\mathrm{SFR(UV)}_{\mathrm{corrected}}$ in bins of $\mathrm{SFR(UV)}_{\mathrm{corrected}}$. The colors denote different recipes for the nebular dust correction. Using the same color excess for nebular extinction together with the Calzetti curve (model D; see text) gives the best agreement between Hα and UV SFRs, while assuming higher nebular attenuation (i.e., $E(B-V)_{\mathrm{nebular}} = 2.27\,E(B-V)_{\mathrm{stellar}}$) with the Calzetti curve results in SFR(Hα) that is significantly larger than SFR(UV) (model A). The details of each model are summarized in Table 2.

Table 2
Dust Corrected Hα SFRs Using Different Attenuation Recipes, in Bins of $\mathrm{SFR(UV)}_{\mathrm{corr}}$

$\mathrm{SFR(UV)}_{\mathrm{corr}}$[a]	N[b]	$\mathrm{SFR(H}\alpha)_{\mathrm{corr}}$[c]				
		Calzetti Different $E(B-V)$[d] (Model A)	Galactic Different $E(B-V)$[e] (Model B)	SMC Different $E(B-V)$[f] (Model C)	Calzetti Equal $E(B-V)$[g] (Model D)	Galactic Equal $E(B-V)$[h] (Model E)
18 ± 3	26	44 ± 3	38 ± 3	34 ± 2	30 ± 2	28 ± 2
32 ± 6	63	70 ± 4	54 ± 3	46 ± 3	38 ± 2	35 ± 2
65 ± 12	83	103 ± 7	75 ± 5	61 ± 4	49 ± 3	43 ± 3
120 ± 22	56	200 ± 18	140 ± 12	112 ± 10	88 ± 8	76 ± 7
258 ± 94	15	443 ± 88	295 ± 59	228 ± 45	174 ± 35	146 ± 29

[a] The mean and standard deviation of the corrected SFR(UV) in each bin, in units of $M_\odot$ yr^{-1}.
[b] Number of objects in each bin.
[c] The $\mathrm{SFR(H}\alpha)_{\mathrm{corr}}$ is derived based on the stacked SEDs in bins of dust-corrected SFR(UV), in units of $M_\odot$ yr^{-1}. The errors are 1σ standard error of the mean of the K_s magnitudes contributing to each bin, which is converted to the error in SFR.
[d] $A_{\mathrm{H}\alpha} = 2.27\,\kappa_{\mathrm{Calz}}(\mathrm{H}\alpha)E(B-V)_{\mathrm{stellar}}$; $A_{\mathrm{H}\alpha}$ is the total nebular extinction at 6564 Å and $\kappa_{\mathrm{Calz}}(\mathrm{H}\alpha)$ is the Calzetti reddening at 6564 Å.
[e] $A_{\mathrm{H}\alpha} = 2.27\,\kappa_{\mathrm{Gal}}(\mathrm{H}\alpha)E(B-V)_{\mathrm{stellar}}$; $\kappa_{\mathrm{Gal}}(\mathrm{H}\alpha)$ is the Cardelli Galactic reddening at 6564 Å.
[f] $A_{\mathrm{H}\alpha} = 2.27\,\kappa_{\mathrm{SMC}}(\mathrm{H}\alpha)E(B-V)_{\mathrm{stellar}}$; $\kappa_{\mathrm{SMC}}(\mathrm{H}\alpha)$ is an SMC reddening at 6564 Å.
[g] $A_{\mathrm{H}\alpha} = \kappa_{\mathrm{Calz}}(\mathrm{H}\alpha)E(B-V)_{\mathrm{stellar}}$; $\kappa_{\mathrm{Calz}}(\mathrm{H}\alpha)$ is the Calzetti reddening at 6564 Å.
[h] $A_{\mathrm{H}\alpha} = \kappa_{\mathrm{Gal}}(\mathrm{H}\alpha)E(B-V)_{\mathrm{stellar}}$; $\kappa_{\mathrm{Gal}}(\mathrm{H}\alpha)$ is the Cardelli Galactic reddening at 6564 Å.

extinction of the Hα emission line, and $E(B-V)_{\mathrm{stellar}}$ is the SED-inferred stellar color excess.

We investigate several of the more commonly used dust-correction recipes, as described below. The Hα SFRs are corrected using five different methods:

a. the Calzetti attenuation curve for both gas and stars, but 2.27× larger color excess for the nebular lines than the stellar continuum (as we call it "different $E(B-V)$");
b. the Calzetti attenuation curve for the stellar continuum, and the Cardelli et al. (1989) Galactic curve for the nebular lines assuming 2.27× larger color excess;
c. the Calzetti attenuation curve for the stellar continuum, and an SMC extinction curve (Gordon et al. 2003) for the nebular lines assuming 2.27× larger color excess;
d. the Calzetti attenuation curve for both gas and stars, and the same color excess (as we call it "equal $E(B-V)$"); and
e. the Calzetti attenuation curve for the stellar continuum, an SMC extinction curve (Gordon et al. 2003) for the nebular lines assuming the same color excess.

We choose to compare these different dust-correction scenarios for the stacked values instead of the individual galaxies as the former represent an average over many points including both detected and undetected quantities, each of which may be relatively uncertain. The results are plotted in the right panel of Figure 4 and are reported in Table 2.

To summarize, these are the values that are used to correct the observed Hα SFRs in each model according to

Equation (4):

$$A_{\rm H\alpha}^{(A)} = 2.27\ \kappa_{\rm Calz}({\rm H}\alpha)E(B-V) = 7.56\,E(B-V),$$
$$A_{\rm H\alpha}^{(B)} = 2.27\ \kappa_{\rm Gal}({\rm H}\alpha)E(B-V) = 5.72\,E(B-V),$$
$$A_{\rm H\alpha}^{(C)} = 2.27\ \kappa_{\rm SMC}({\rm H}\alpha)E(B-V) = 4.54\,E(B-V),$$
$$A_{\rm H\alpha}^{(D)} = \kappa_{\rm Calz}({\rm H}\alpha)E(B-V) = 3.33\,E(B-V),$$
$$A_{\rm H\alpha}^{(E)} = \kappa_{\rm Gal}({\rm H}\alpha)E(B-V) = 2.52\,E(B-V). \quad (5)$$

In these equations, $E(B-V)$ is the SED-inferred color excess observed for the stellar continuum and $A_{\rm H\alpha}$ is the total nebular extinction at 6564 Å.

In model (A) with a larger color excess for the nebular regions with the Calzetti curve, Hα-inferred SFRs are significantly larger than UV SFRs. Taking the average of the SFR(Hα) (model A) to the corrected SFR(UV) in the five bins of SFR(UV) indicated in Table 2 yields a value of 2.1 ± 0.2, which shows a $\sim 5\sigma$ discrepancy from unity.

Using either model (C) or (D) results in $\rm SFR_{corrected}(H\alpha)$ that are in good agreement with $\rm SFR_{corrected}(UV)$. Model (B) reproduces systematically higher SFRs but is still consistent with the range of $\rm SFR_{corrected}(UV)$ in higher bins, and model (E) estimations are lower than expected.

Based on the data provided in Table 2 and the right panel of Figure 4, model (D) provides the best agreement between SFRs among the five models. The average of the SFR(Hα)-to-SFR (UV) ratios in the five SFR(UV) bins of this model shows less than 1σ discrepancy from unity. This suggests that *on average* the best recipe to correct the Hα-inferred quantities of star-forming galaxies at $z \sim 2$ is to use $E(B-V)_{\rm nebular} = E(B-V)_{\rm stellar}$ with the Calzetti reddening curve.

6. BOLOMETRIC SFRs

As discussed above, a primary disadvantage of using Hα and UV SFR diagnostics is that we must account for dust extinction, though this is less of a problem for Hα as it is for the UV. The attenuation curves (e.g., the Calzetti et al. 2000 curve) that are used to correct the luminosities encode information regarding the dust grain size distribution and the geometrical distribution of dust with respect to stars (e.g., whether the dust is clumpy or uniform, a homogeneous mixture or a foreground screen, etc). On the other hand, the IR luminosity is a direct tracer of dust and thus provides an independent and more robust diagnostic of dust attenuation.[7] Adding the IR luminosity, which accounts for the obscured star formation, to the unobscured (UV and Hα) tracers of SFR can give a more reliable estimate of the bolometric SFR.

6.1. The Relationship between Observed Hα Luminosity and Total SFR

To convert the observed Hα luminosity to total SFR, the most commonly used calibration is that of Kennicutt (1998), which is computed using an evolutionary synthesis model, assuming Case B recombination with $T_e = 10{,}000$ K. In the absence of Balmer decrement measurements, the observed Hα SFR must be corrected for dust with some assumption of the attenuation curve and color excess of the ionized gas. In this section, we examine the $L_{\rm H\alpha}$-to-SFR conversion by relying only on the observed data, without making any assumptions about the dust correction or electron temperature of the ionized gas. With this conversion, one can use the Hα observed luminosity as a proxy for total SFR without assuming a dust attenuation curve and its associated uncertainties. The conversion applies to stellar populations with constant star formation at least over 100 Myr. For bursty star formation histories over timescales shorter than 100 Myr, the Hα and UV+IR luminosities diverge as the Hα luminosity traces more instantaneous star formation over timescales of ∼10 Myr, while IR+UV is not sensitive to the change of star formation on timescales $\lesssim$100 Myr. Here, we are deriving the conversion factor based on the stacked data that represents the "average" quantities and thus should be used with caution for galaxies that may be undergoing bursty star formation.

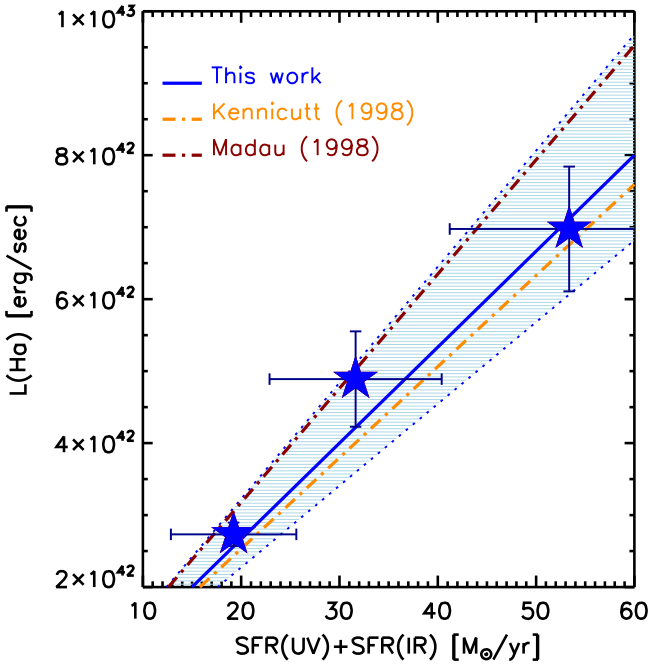

Figure 5. Observed Hα line luminosity as a function of bolometric SFR. The stars indicate the average values in bins of SFR(SED). Galaxies with SFR (SED) < 32 $M_\odot$ yr^{-1} are in the first bin; those with SFR(SED) between 32 and 100 $M_\odot$ yr^{-1} are in the middle bin; and the last bin consists of galaxies with SFR(SED) > 100 $M_\odot$ yr^{-1}. The error in SFR(UV)+SFR(IR) is determined by the dispersion error in IR luminosity of the objects contributing to each stack. L(IR) dispersion error is estimated through bootstrap resampling simulations. The solid blue line is the best linear fit. The slope of this fit gives us the conversion factor for the $L({\rm H}\alpha)_{\rm obs}$-to-$\rm SFR_{total}$ relation. The shaded area is the 68% confidence interval of our estimated slope. The orange and dark-red dashed lines show the conversion factors of Kennicutt (1998) and Madau et al. (1998), respectively.

Bolometric SFR (SFR(IR)+SFR(UV)) is plotted as a function of the Hα luminosity in Figure 5. As both the Hα and IR measurements have non-detections, we decided to bin the data with respect to the SED-inferred SFR. We chose the bins so that in each bin the SFR(SED) is consistent with the stacked SFR(IR)+SFR(UV) within the uncertainties, because ultimately we are using SFR(IR)+SFR(UV) to calculate the Hα luminosity-to-SFR conversion factor. MIPS data are stacked in each bin and the total IR luminosity is extracted in

[7] The dust heated by the visible light from older stellar populations (i.e., the cold component) also contributes to the IR luminosity. However, in case of the star-forming galaxies the contribution of the UV radiation of massive stars (the warm component) is expected to dominate the total IR luminosity (Kennicutt 1998).

the same way as for individual galaxies. The UV and Hα luminosities are derived from the stacked SEDs.

A weighted least-squares regression method is used to find the slope of the relation:

$$\mathrm{SFR_{bol}}\left(M_\odot\ \mathrm{yr^{-1}}\right) = (7.5 \pm 1.3) \times 10^{-42}\, L_{\mathrm{obs}}(\mathrm{H}\alpha)\ \left(\mathrm{erg\ s^{-1}}\right). \quad (6)$$

This relation can be used to convert the observed Hα luminosity in units of erg s^{-1} to the bolometric SFR. The factor given in Kennicutt (1998) and Kennicutt et al. (1994), to convert observed/intrinsic luminosity to observed/intrinsic SFR, is 7.9×10^{-42} $M_\odot\ \mathrm{yr^{-1}\ erg^{-1}\ s}$. Madau et al. (1998) reported a conversion factor of 6.3×10^{-42} $M_\odot\ \mathrm{yr^{-1}\ erg^{-1}\ s}$. These factors are computed using evolutionary synthesis models and are subject to those models' uncertainties, as well as the initial assumptions that went into these models, such as IMF, star-formation history, and the stellar evolution and atmosphere models. For the same galaxy type and assumed IMF, Kennicutt (1998) reports ∼30% variation among different calibrations, which mainly reflects the sensitivity to the SED modeling stellar evolution input data. In our analysis, converting L(IR) and L(UV) to SFR still relies on the model assumptions, but previous studies have shown that in the absence of the Balmer decrement measurements, the sum of SFR(IR) and SFR(UV) is the most reliable estimate of total SFR (Hirashita et al. 2003; Reddy et al. 2012b). Our derived slope for a Salpeter IMF is consistent with Kennicutt (1998) and Madau et al. (1998) within the errors.

Excluding galaxies with ages <100 Myr (see Section 6.2) results in a best-fit slope of 7.8×10^{-42} $M_\odot\ \mathrm{yr^{-1}\ erg^{-1}\ s}$ that is consistent with the slope found above.

6.2. Validity of the Calzetti Dust Attenuation for Young Galaxies

Figure 6 shows the bolometric SFR versus median SFR inferred from the best-fit SED model, in bins of SFR(SED). Both quantities are representative of the total SFR of the galaxies, the only difference being the method by which dust is accounted for. The bolometric SFR, as mentioned before, is the sum of SFR(IR) and SFR(UV) and is independent of any dust correction. On the other hand, for SFR(SED), the effect of dust is considered by using the Calzetti attenuation curve in the SED fitting procedure. We would like to determine whether for all types of galaxies at $z \sim 2$ the bolometric SFRs agree with SED SFRs that are corrected by the Calzetti attenuation curve. We stack the MIPS data of individual detected and undetected galaxies in three bins of SFR(SED) as described in Section 2.3. The three bins in log(SFR(SED)) are <1.5, 1.5–2, and >2, with respectively 44, 56, and 15 galaxies in each bin. SFR(SED) and SFR(UV) are the median SFRs of the individual galaxies in each bin. The results of stacking are shown with open blue circles in Figure 6. In the last two bins, the SED SFR is overestimated compared to the bolometric SFR. Stacking the MIPS images for only objects that are inferred to be older than 100 Myr produces different results. The number of objects in bins with galaxies older than 100 Myr reduces to 43, 50, and 8, respectively, from the lowest SFR(SED) bin to the highest.

Once we remove galaxies with ages <100 Myr, SFR(SED) agrees well with SFR(UV)+SFR(IR). An age-dependent L(UV)-to-SFR calibration (as we use here) does not decrease the difference between SFR(SED) and the bolometric SFR for stacks of all galaxies. It seems that younger galaxies are at the same time less dusty (smaller bolometric SFR) but redder (larger SFR(SED)) than their older counterparts. These results are consistent with those of Reddy et al. (2006b, 2010) and Wuyts et al. (2012), who find that galaxies with young stellar population ages are less dusty for a given UV slope than older galaxies. An SMC-like curve may be more appropriate for these galaxies. One possibility is that young galaxies have larger dust covering fractions than older galaxies (Reddy et al. 2010). A large dust covering fraction makes the UV slope redder for a given amount of dust attenuation. This study confirms that at $z \sim 2$ the Calzetti attenuation curve is applicable to star-forming galaxies older than 100 Myr, but a steeper attenuation curve may be necessary for the younger galaxies.

7. SUMMARY

We have studied the multi-wavelength properties of a sample of ∼200 galaxies with spectroscopically confirmed redshifts at $2.08 \leqslant z \leqslant 2.51$, to study the validity of commonly used dust correction recipes and to compare SFRs inferred from the Hα line luminosity, the UV continuum luminosity, and *Spitzer*/MIPS 24 μm measurements that are converted to the total IR luminosity. In this study, we benefit from using the broadband photometry excess techniques to determine the Hα fluxes and, hence, conduct a large sample of $z \sim 2$ Hα measurements that is immune to uncertainties in the spectroscopic slit-loss corrections. The galaxies' properties are determined from stellar population model fitting to the rest-frame UV through near-infrared data. The main conclusions are as follows:

1. By investigating several recipes for dust correcting the nebular emission lines, we find that assuming the same color excess of the ionized gas and the stellar continuum (i.e., $E(B-V)_{\mathrm{neb}} = E(B-V)_{\mathrm{stel}}$), and assuming that the Calzetti attenuation curve applies to both, results in the best agreement between SFR(Hα) and SFR(UV). If we assume the Calzetti curve to both the stellar and nebular regions but use $E(B-V)_{\mathrm{nebular}} = 2.27\ E(B-V)_{\mathrm{stellar}}$, the corrected SFR(Hα) measurements are inconsistent with the corrected SFR(UV) values at the $\sim 5\sigma$ level, averaged on the five bins of SFR(UV) (see the right panel of Figure 4).
2. Using the available *Spitzer*/MIPS data for ∼100 galaxies in our sample, we derive an observed $L_{\mathrm{H}\alpha}$-to-$\mathrm{SFR_{total}}$ conversion factor of $(7.5 \pm 1.3) \times 10^{-42}$ $M_\odot\ \mathrm{yr^{-1}\ erg^{-1}\ s}$. This calibration is independent of any assumptions on the dust correction and can be used to convert the observed (extincted) Hα luminosity to a bolometric SFR when no dust attenuation measurements for the Hα luminosity are available.
3. By comparing the stacks of SFR(UV)+SFR(IR) with the SED-inferred SFRs that are corrected for dust by the locally derived Calzetti curve, we conclude that a steeper attenuation curve (such as an SMC curve) may be necessary for galaxies younger than 100 Myr, as previous studies (Reddy et al. 2006b, 2010; Wuyts et al. 2012) have found. We find that applying the Calzetti curve to the stacks of all galaxies, including the young ones, results in SFR(SED) values that are inconsistent with the SFR(UV) +SFR(IR) at $\sim 2\sigma$ significance (the SFR(SED) in three

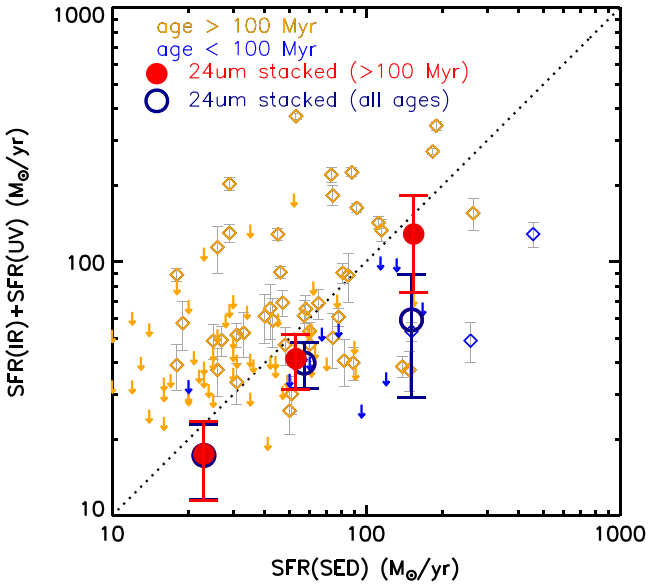

Figure 6. Comparison of the bolometric SFR and SED-inferred SFR. The values are divided into three bins of SFR(SED) including individual detections and individually undetected galaxies at 24 μm; open blue circles include all objects, and filled red circles include only those galaxies older than 100 Myr. Diamonds are individual detected objects, and downward arrows represent 3σ upper limits in SFR(IR)+SFR(UV) for the MIPS undetected galaxies. Young galaxies (ages < 100 Myr) are colored blue, and galaxies with ages > 100 Myr are orange. SFR(IR) error bars are estimated through bootstrap simulations and show the dispersion in the SFRs contributing to each stack. The last bin consists of galaxies with SFR(SED) > 100 $M_\odot$ yr^{-1}; by removing young galaxies (ages < 100 Myr), about half of the sample in this bin is dismissed and we see the change between the two measurements (including and excluding the young ones). The dotted line indicates a one-to-one correspondence.

mass bins of Figure 6 are inconsistent with SFR(UV) +SFR(IR) by 1σ, 2σ, and 3σ, from the lowest to highest mass bins, respectively). The young galaxies have redder UV slope and at the same time lower bolometric SFR compared to their older counterparts. As a result, applying the Calzetti curve to the young galaxies overestimates the SED-inferred SFR when compared with their bolometric SFR. The Calzetti attenuation curve shows a good overall agreement for galaxies older than 100 Myr.

A more detailed investigation will include direct tracers of nebular dust extinction (i.e., the Balmer decrement). In future studies, we plan to investigate this aspect with the MOSFIRE Deep Evolution Field (MOSDEF) survey, which uses the near-IR multi-object spectrograph MOSFIRE on the Keck I telescope to obtain spectroscopic measurements of the nebular emission lines for a sample of ≈1500 galaxies (Kriek et al. 2014).

I.S. thanks Valentino González for useful discussions. Support for I.S. is provided through the National Science Foundation Graduate Research Fellowship under Grant No. DGE-1326120. N.A.R. is supported by an Alfred P. Sloan Research Fellowship.

REFERENCES

Adelberger, K. L., Steidel, C. C., Shapley, A. E., et al. 2004, ApJ, 607, 226
Bouwens, R. J., Illingworth, G. D., Oesch, P. A., et al. 2010, ApJL, 709, L133
Calzetti, D., Armus, L., Bohlin, R. C., et al. 2000, ApJ, 533, 682
Calzetti, D., Kinney, A. L., & Storchi-Bergmann, T. 1994, ApJ, 429, 601
Cardelli, J. A., Clayton, G. C., & Mathis, J. S. 1989, ApJ, 345, 245
Chary, R., & Elbaz, D. 2001, ApJ, 556, 562
Cid Fernandes, R., Mateus, A., Sodré, L., Stasinska, G., & Gomes, J. M. 2005, MNRAS, 358, 363
Dale, D. A., & Helou, G. 2002, ApJ, 576, 159
De Barros, S., Schaerer, D., & Stark, D. P. 2014, A&A, 563, A81
Dickinson, M., Giavalisco, M., & The Goods Team 2003, in The Mass of Galaxies at Low and High Redshift, ed. R. Bender & A. Renzini (Berlin: Springer), 324
Elbaz, D., Dickinson, D., Hwang, H. S., et al. 2011, A&A, 533, 119
Erb, D. K., Shapley, A. E., Pettini, M., et al. 2006a, ApJ, 644, 813
Erb, D. K., Steidel, C. C., Shapley, A. E., et al. 2006b, ApJ, 647, 128
Fioc, M., & Rocca-Volmerange, B. 1997, A&A, 326, 950
Förster Schreiber, N. M., Genzel, R., Bouché, N., et al. 2009, ApJ, 706, 1364
Garn, T., Sobral, D., Best, P. N., et al. 2010, MNRAS, 402, 2017
Gordon, K. D., Clayton, G. C., Misselt, K. A., Landolt, A. U., & Wolff, M. J. 2003, ApJ, 594, 279
Guiderdoni, B., & Rocca-Volmerange, B. 1987, A&A, 186, 1
Hirashita, H., Buat, V., & Inoue, A. K. 2003, A&A, 410, 83
Kennicutt, R. C. 1998, ARA&A, 36, 189
Kennicutt, R. C., Tamblyn, P., & Congdon, C. E. 1994, ApJ, 435, 22
Kriek, M., Shapley, A. E., Reddy, N. R., et al. 2014, arXiv:1412.1835
Kriek, M., van Dokkum, P. G., Franx, M., et al. 2007, ApJ, 669, 776
Kriek, M., van Dokkum, P. G., Franx, M., Illingworth, G. D., & Magee, D. K. 2009, ApJL, 705, L71
Law, D. R., Steidel, C. C., Shapley, A. E., et al. 2012, ApJ, 745, 85
Madau, P., & Dickinson, M. 2014, ARA&A, 52, 415
Madau, P., Pozzetti, L., & Dickinson, M. 1998, ApJ, 498, 106
Magnelli, B., Elbaz, D., Chary, R. R., et al. 2011, A&A, 528, A35
Muzzin, A., van Dokkum, P., Kriek, M., et al. 2010, ApJ, 725, 742
Nordon, R., Lutz, D., Shao, L., et al. 2010, A&A, 518, L24
Oke, J. B., & Gunn, J. E. 1983, ApJ, 266, 713
Price, S. H., Kriek, M., Brammer, G. B., et al. 2014, ApJ, 788, 86
Reddy, N. A., Dickinson, M., Elbaz, D., et al. 2012a, ApJ, 744, 154
Reddy, N. A., Erb, D. K., Pettini, M., Steidel, C. C., & Shapley, A. E. 2010, ApJ, 712, 1070
Reddy, N. A., Pettini, M., Steidel, C. C., et al. 2012b, ApJ, 754, 25
Reddy, N. A., & Steidel, C. C. 2009, ApJ, 692, 778
Reddy, N. A., Steidel, C. C., Erb, D. K., et al. 2006a, ApJ, 653, 1004
Reddy, N. A., Steidel, C. C., Fadda, D., et al. 2006b, ApJ, 644, 792
Rieke, G. H., Alonso-Herrero, A., Weiner, B. J., et al. 2009, ApJ, 692, 556
Salpeter, E. E. 1955, ApJ, 121, 161
Schenker, M. A., Ellis, R. S., Konidaris, N. P., & Stark, D. P. 2013, ApJ, 777, 67
Shapley, A. E. 2011, ARA&A, 49, 525
Shapley, A. E., Steidel, C. C., Erb, D. K., et al. 2005, ApJ, 626, 698
Shim, H., Chary, R., Dickinson, M., et al. 2011, ApJ, 738, 69
Stark, D., Schenker, M. A., Ellis, R., et al. 2013, ApJ, 763, 129
Steidel, C. C., Adelberger, K. L., Shapley, A. E., et al. 2003, ApJ, 592, 728
Steidel, C. C., Erb, D. K., Shapley, A. E., et al. 2010, ApJ, 717, 289
Steidel, C. C., Rudie, G. C., Strom, A. L., et al. 2014, ApJ, 795, 165
Steidel, C. C., Shapley, A. E., Pettini, M., et al. 2004, ApJ, 604, 534
van Dokkum, P. G., Kriek, M., Rodgers, B., Franx, M., & Puxley, P. 2005, ApJL, 622, L13
Wild, V., Charlot, S., Brinchmann, J., et al. 2011, MNRAS, 417, 1760
Wuyts, E., Rigby, J. R., Gladders, M. D., et al. 2012, ApJ, 745, 86
Wuyts, S., Förster Schreiber, N. M., Lutz, D., et al. 2011, ApJ, 738, 106
Yoshikawa, T., Akiyama, M., Kajisawa, M., et al. 2010, ApJ, 718, 112
Zackrisson, E., Bergvall, N., & Leitet, E. 2008, ApJ, 676, 9
Zeimann, G. R., Ciardullo, R., Gebhardt, H., et al. 2014, ApJ, 790, 113